Supplementary Information (SI) for Lab on a Chip.

The electronic supplementary information includes:

S1. The adaptive-topology path planning algorithm;
S2. Droplet conflict resolution strategy;
S3. Chip fabrication;
S4. Setup of DMF hardware;
S5. Dataset establishment;
S6. The proposed semantic segmentation model;
S7. Equations of the mean intersection over union, loss, and mean pixel accuracy;
S8. The performance of the proposed semantic segmentation model;
S9. HSV-Based colorimetric analysis for concentration determination;
S10. Mixing operation workflow;
S11. Dynamic path replanning with droplet splitting;

Video S1-6. Size 4 droplet path planning in four directions (video S1); Size 4 droplet path planning in eight directions (video S2); multi-droplet path planning with conflict resolution (video S3); Path planning in the presence of obstacle electrodes (video S4); Path planning with dynamically inserted merging task (video S5); Schematic diagram of solution dilution (video S6).

S1. The adaptive-topology path planning algorithm

Table 1 The pseudocode of the adaptive-topology A* algorithm.

Algorithm: Adaptive-topology A* algorithm for multi-electrode droplets

Input: Chip graph $G(V,E)$, droplet set D, $starting\_point[]$, $ending\_point[]$, $deformation\ threshold\ \delta$

Output: Conflict-free path set Paths

```
Initialize path set Paths = {}
For each droplet $d_i \in D$:
    Initialize $OpenList = \{\}$, $ClosedList = \{\}$
    Add initial $state\ (e_{lead}, S_i^t)$ to OpenList
    $e_{lead} = argmin\ distance(e, ending\_point[i]) \big| (e \in S_i^t))$
    While OpenList not empty:
        current = extract state with minimum $f - value$ from OpenList
        If current $e_{lead}$ reaches $ending\_point[i]$:
            Reconstruct path and add to Paths; break
        For each adjacent position $p_i^t$ of current $e_{lead}$:
            // Generate topology configurations with new leading vertex at $p_i^t$
            $T_i^t$ = generate_topologies ($S_i^t$, $p_i^t$)
            For each topology $S_i^t \in T_i^t$:
                // Validate connectivity constraint
                If not is_connected_subgraph ($S_{i'}^t$):
                    continue
                // Validate deformation constraint
                If $\left| T_i^t \triangle T_i^{t+1} \right| > \delta$:
                    continue
                // Validate collision avoidance
                collision = false
                For each other droplet $dj \in D, j \neq i$:
                    For each electrode $e_a \in S_i^t$, $e_b \in S_j^t$:
```

```
                        If Chebyshev_distance$(e_a, e_b) < d_{safe}$:
                            collision = true; break
                If not collision:
                    Calculate $g' = g$
                    Calculate $h' = manhattan\_distance(p_i^t, ending\_point[i])$
                    Calculate $\varphi = topology\_adaptation\_cost$
                    $f = g + h' + \varphi$
                    Add or update state $(p_i^t, S_i^{t'})$ in OpenList with $f$
        Move current to ClosedList
Return Paths
```

S2. Droplet conflict resolution strategy

As illustrated in Fig. S1a, a path crossing conflict occurs when two droplets' trajectories intersect at a common node during their movement. In this scenario, Droplet 1 moves horizontally to the right while Droplet 2 moves vertically downward. The red dashed box indicates the conflict point where both droplets' paths converge, creating a potential collision risk.

For path crossing conflicts, we employ a domain-knowledge-guided sequential movement strategy. Instead of relying on geometric metrics like path length, priorities are pre-assigned by experts based on the biochemical nature of the droplets. Droplets containing sensitive biological samples or time-critical reagents are designated as "High Priority," while droplets containing buffers or waste are designated as "Low Priority."

In the example of Fig. S1a, assuming Droplet 1 contains a critical reagent (High Priority), it is allowed to occupy the conflict node first. Droplet 2 (Low Priority) must wait until Droplet 1 has completely passed through the conflict zone before proceeding. This ensures that critical biochemical steps are prioritized.

Fig. S1b demonstrates a destination conflict scenario where Droplet 1 and Droplet 2 move toward overlapping destination areas. To resolve this, we implement a priority-based path replanning algorithm:

(1) Priority Assessment: The system retrieves the pre-configured priority levels of the conflicting droplets.

(2) Strategy Execution: The droplet with lower biochemical priority (e.g., Droplet 2) is selected as the candidate for replanning.

(3) Replanning: A modified A* algorithm generates an alternative route for the lower-

priority droplet to circumvent the high-priority droplet's path or destination.

As shown in Fig. S1b, the low-priority Droplet 2 executes a detour (e.g., moving upward) to avoid the conflict area, ensuring that the high-priority Droplet 1 can proceed along its optimal path without delay. This approach effectively translates biological protocol constraints into automated control logic..

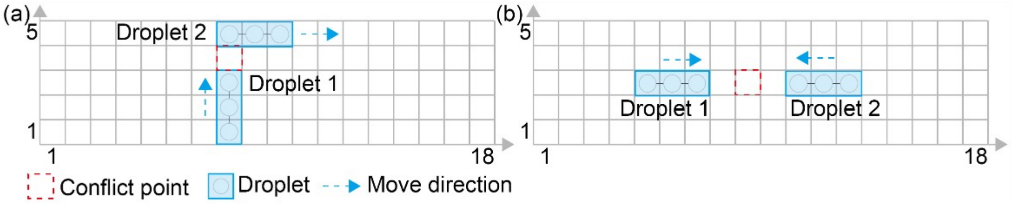

Fig. S1 Conflict types during droplet movement in DMF. (a) After the droplet turns, it does not meet the distance constraint and conflicts; (b) Droplets move towards each other, causing conflicts in their paths.

S3. Chip fabrication

The DMF chip from Renx Biotechnology Co., Ltd. (Shanghai, China) consists of a bottom plate and a top plate, with the latter integrated with multiple PRS. The bottom plate contains a silver electrodes array, with a PET film covered atop as the dielectric layer. The electrode array consists of 128 actuation electrodes (1.76 × 1.76 mm) and 10 reservoir electrodes (5.4 × 5.4 mm), with electrode gap of 20 μm. The top plate was fabricated by firstly spin-coating CYTOP onto an ITO glass, and baked at 135°C for 20 min, forming the hydrophobic layer. Finally, the two plates were assembled with a 350 μm thick plastic frame as spacer, which would lead to the estimated droplet volumes of 1.7 μL and 10 μL on the actuation and reservoir electrodes, respectively. For droplets manipulation on DMF, the chip was firstly filled with silicone oil, and applied the voltage of 95 Vrms (100 Hz).

S4. Setup of DMF hardware and operational parameters

A homemade DMF system was used to manipulate the DMF chip and control the droplet manipulation processes. A 1080p USB camera was positioned above the DMF chip to observe and capture images of droplet manipulation. The resolution of the camera was set to 1920 × 1080 to obtain clear images. The images were then transmitted to a computer equipped with an R7 9800X3D CPU, 32 GB RAM, and RTX 4080SUPER GPU for further processing and analysis.

To initiate the automated workflow of the TDMC system, several core logical parameters must be provided as inputs by the user. These include the identity and initial configuration of droplets, specifically the total number of droplets, their size, their unique IDs, and their respective starting coordinates on the array. Furthermore, task assignments must be provided to specify the destination or functional site (such as dispensing or mixing points) for each identified droplet. Once these logical inputs are integrated, the system automatically invokes the ATA algorithm to generate coordinated global routing paths for each identified droplet. In addition to these logical requirements, basic physical and adjustable parameters are configured to ensure stable actuation, including an actuation voltage of 95 V (AC, 200 Hz, square wave) and an actuation duration of 1 s as applied in our experiments.

S5. Dataset establishment

A droplet dataset was established with a digital camera. Images of various droplet manipulations were captured with frame rate of 30 frames per second. The captured videos were converted into a series of images (1920 × 1080) with OpenCV. The dataset was divided into training and validation sets in a ratio of 0.8:0.2, including 3503 images in the training set and 876 images in the validation set. The training set was used to train the model, and the validation set was used to evaluate the model's performance. The dataset had been made public for others. This protocol can be used as a reference for establishing other DMF droplet manipulation datasets.

S6. The proposed semantic segmentation model

A deep learning algorithm for the automatic segmentation of droplet path planning is proposed (Fig. S2). The model is based on a U-net encoder-decoder architecture, where feature extraction is performed by the encoder and upsampling by the decoder. Corresponding feature maps between encoder and decoder are connected via skip connections, allowing both high- and low-level features to be captured.

The decoder uses 8 convolutional layers paired with upsampling and transpose convolutions to restore feature maps to the input size. Skip connections retain spatial details by connecting encoder and decoder feature maps of the same resolution, improving segmentation accuracy. The network ends with a 1 × 1 convolutional layer outputting two channels, matching the number of label categories and ensuring precise segmentation results.

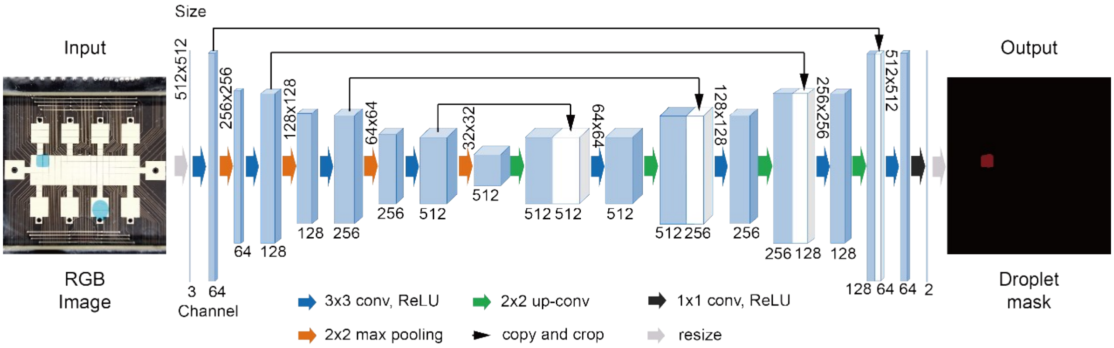

Fig. S2 The overall structure of semantic segmentation model.

S7. Equations of the mean intersection over union, loss, and mean pixel accuracy

The mean intersection over union (mIoU) was employed as the evaluation indicator for the semantic segmentation performance (Eq.1). This metric is the average of the ratio of the intersection and union of various real labels and prediction results.

$$mIoU = \frac{1}{n+1}\sum_{i=0}^{n}\frac{p_{ii}}{\sum_{j=0}^{n} p_{ij} + \sum_{j=0}^{n} p_{ji} - p_{ii}}$$

* MERGEFORMAT

(1)

where n represents the total number of categories, p_{ii} represents the number of correct predictions, p_{ij} represents false negatives, in which i is predicted as j, and p_{ji} represents false positives.

The Dice loss was employed as the loss function (Eq.2). A lower value of Dice loss, indicates greater similarity between the predicted and ground truth results.

$$loss = 1 - 2\times\frac{|x \cap y|}{|x| + |y|}$$

* MERGEFORMAT

(2)

where x represents the predicted segmentation mask and y represents the ground truth segmentation mask.

The mean pixel accuracy (mPA) refers to comparing each pixel predicted by the model with its corresponding ground truth label and calculating the ratio of correctly classified pixels to the total number of pixels, calculated as Eq.3.

$$mPA = \frac{1}{n+1}\sum_{i=0}^{n}\frac{p_{ii}}{\sum_{j=0}^{n} p_{ij}}$$

* MERGEFORMAT (3)

where, n represents the total number of categories, p_{ii} represents the number of correct predictions, p_{ij} represents predicting of i as j, false negatives.

S8. The performance of the proposed semantic segmentation model

To validate the segmentation performance of the proposed model on our dataset, the model segmentation results, mIoU, loss, and mPA are provided to analyze its performance. The mIoU indicates the extent to which the model-predicted area overlaps with the actual area. The loss is used to measure the difference between the model prediction and the actual target. The mIoU of the validation set for the semantic segmentation model is 97.08% (Fig. S3a). A high mIoU indicates better segmentation performance, with the model predicted regions overlapping more closely with the actual regions. Moreover, the loss of the validation set for the proposed stabilizes at 0.08 (Fig. S3b). The loss indicates that the state predictions of the proposed are closer to the true droplet states. The mPA evaluates the percentage of correctly classified pixels across all classes, providing a pixel-level accuracy assessment. The validation set achieves a mPA of 96.81% (Fig. S3c), which confirms the model strong performance in pixel-level classification accuracy.

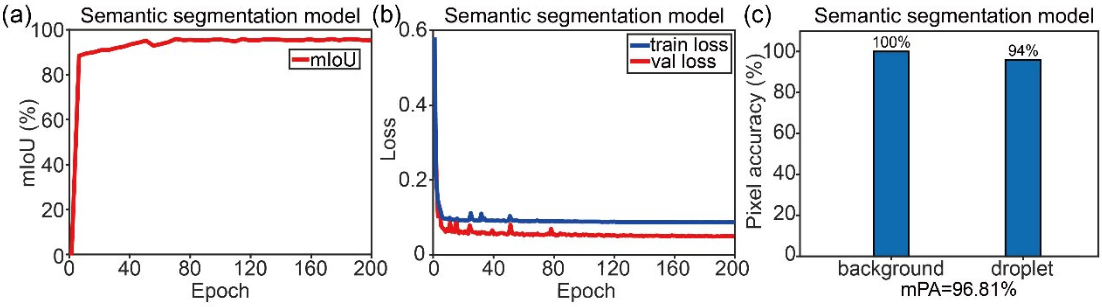

Fig. S3(a) Semantic segmentation model mIoU. (b) Training and validation loss. (c) Semantic segmentation model mPA.

S9. HSV-Based colorimetric analysis for concentration determination

To quantitatively validate the precision of the automated on-chip dilution, we employed colorimetric analysis based on the HSV (Hue, Saturation, Value) color space. Unlike RGB, the HSV model decouples chromaticity (Hue and Saturation) from luminosity (Value), providing a more robust metric for concentration analysis under varying lighting conditions [1]. Pixel values were extracted from the center of the droplet images and converted from RGB to HSV coordinates using the OpenCV library.

We evaluated the sensitivity of the three components (H, S, V) to changes in solution concentration (25% to 75%).

1. Hue (H) and Saturation (S): As detailed in Table S3, the Hue (H) remained stable across all concentrations (Merged: 185.4° ± 8.0°; Original: 186.0° ± 8.4°). Statistical analysis showed no significant correlation between H and concentration ($r = +0.12$, $p = 0.76$), which is expected as the fundamental color type (cyan-blue) does not shift during dilution. Similarly, the Saturation (S) exhibited a "ceiling effect," consistently approaching 100% (Range: 98.6% – 99.7%). This occurs because the stock solution is inherently dark with low RGB values. Mathematically, as the minimum RGB component approaches zero, the saturation formula $S = (\mathrm{Max} - \mathrm{Min}) / \mathrm{Max} \times 100\%$ asymptotes to 100%, rendering it insensitive to concentration changes in this context.

2. Value (V): In contrast, the Value (V), representing brightness, demonstrated a wide dynamic range from 18.4% to 53.4%. As shown in Fig. 6f and Table S3, there is a strong negative linear correlation between the V-value and concentration ($r = -0.9961$, $R^2 = 0.9922$, $p < 0.001$). This aligns with the Beer-Lambert law [2], where increased solute concentration leads to higher light absorption and consequently lower brightness.

Based on these findings, the V-parameter was selected as the optimal indicator for concentration determination because: (1) it offers a broad dynamic range (35% span vs. <2% for H/S); (2) it exhibits high linearity with concentration; and (3) it avoids the artifacts affecting H (constancy) and S (ceiling effect). The stability of the control group (Original Solution) further confirms that variations in V were solely due to the automated dilution process.

Table S2. Representative HSV measurements from a single image

Sample Point	RGB Values	H (°)	S (%)	V (%)
Merged Solution				
Point 1	(0, 43, 50)	188.0	100.0	19.6
Point 2	(0, 52, 63)	190.0	100.0	24.7
Point 3	(0, 38, 49)	194.0	100.0	19.2
Mean ± SD		190.7 ± 2.3	100.0 ± 0.0	21.2 ± 2.5
Original Solution				
Point 4	(0, 13, 18)	196.0	100.0	7.1
Point 5	(1, 13, 9)	160.0	92.2	5.1
Point 6	(0, 9, 16)	206.0	100.0	6.3
Mean ± SD		187.3 ± 20.7	97.4 ± 4.4	6.1 ± 0.9
Difference		+3.4°	+2.6%	+15.0%

Table S3. Summary statistics across all concentration ratios (n = 2084 images total)

Concentration (%)	Merged H (°)	Merged S (%)	Merged V (%)	Original H (°)	Original S (%)	Original V (%)
25.0	184.5 ± 8.2	99.7 ± 0.3	53.4 ± 1.3	186.2 ± 9.5	98.6 ± 0.3	5.9 ± 0.3
33.3	186.1 ± 7.8	99.7 ± 0.3	48.2 ± 1.2	185.8 ± 8.9	99.3 ± 0.5	5.8 ± 0.5
40.0	185.9 ± 8.1	99.7 ± 0.3	43.4 ± 1.8	186.5 ± 9.2	99.3 ± 0.6	6.2 ± 0.6
42.9	186.3 ± 8.4	99.7 ± 0.3	40.8 ± 1.1	186.1 ± 8.7	98.9 ± 0.1	5.9 ± 0.1
50.0	185.8 ± 7.5	99.3 ± 0.7	37.6 ± 1.1	185.9 ± 8.3	99.4 ± 0.7	5.9 ± 0.7
57.1	186.4 ± 8.5	99.4 ± 0.5	33.3 ± 1.6	186.2 ± 8.8	99.4 ± 0.3	5.9 ± 0.3
60.0	186.0 ± 7.9	99.6 ± 0.4	31.2 ± 0.7	185.7 ± 8.6	99.1 ± 0.6	6.1 ± 0.6
66.7	185.4 ± 8.0	99.4 ± 0.6	26.6 ± 0.9	186.0 ± 8.4	99.6 ± 0.3	6.1 ± 0.3
75.0	185.9 ± 7.6	98.6 ± 0.7	18.4 ± 1.2	185.8 ± 8.5	98.6 ± 1.0	6.1 ± 1.0

Reference

[1] Li, Libin, et al. Intelligent droplet tracking with correlation filters for digital microfluidics. Chinese Chemical Letters 32.11 (2021): 3416-3420.

[2] Mayerhöfer, Thomas G., Susanne Pahlow, and Jürgen Popp. The Bouguer‐Beer‐Lambert law: Shining light on the obscure. ChemPhysChem 21.18 (2020): 2029-2046.

S10. Mixing operation workflow

The mixing operation is pre-programmed as a discrete control event within the automated workflow, as illustrated in Fig. S6. Prior to execution, the user defines a mixing region by specifying a set of interconnected electrode nodes on the array. Once all droplets arrive at the designated region, as confirmed by the semantic segmentation model, the system automatically triggers the mixing routine. During mixing, the electrodes within the designated region are sequentially activated and deactivated in a predefined order, driving the merged droplet in a reciprocating motion. Each actuation interval is fixed at 1 s, and the routine is executed for 10 cycles based on empirical optimization. Upon completion, the ATA algorithm generates a new routing path to transport the droplet to its next destination.

S11. Dynamic path replanning with droplet splitting

Fig. S7 depicts a case where a 2U and a 3U droplet are originally routed from their respective start points to designated destinations. At Step 7, a splitting task is dynamically inserted for the blue droplet, as indicated by the green dashed box. At Step 8, the blue droplet executes the splitting operation at its current position and is split into two independent 1U droplets. The two resulting droplets are then treated as independent entities and assigned new destinations respectively, after which the ATA algorithm is re-invoked to replan the paths for all droplets under the updated constraints. By Step 12, both the split blue droplets and the red droplet have reached their respective destinations.

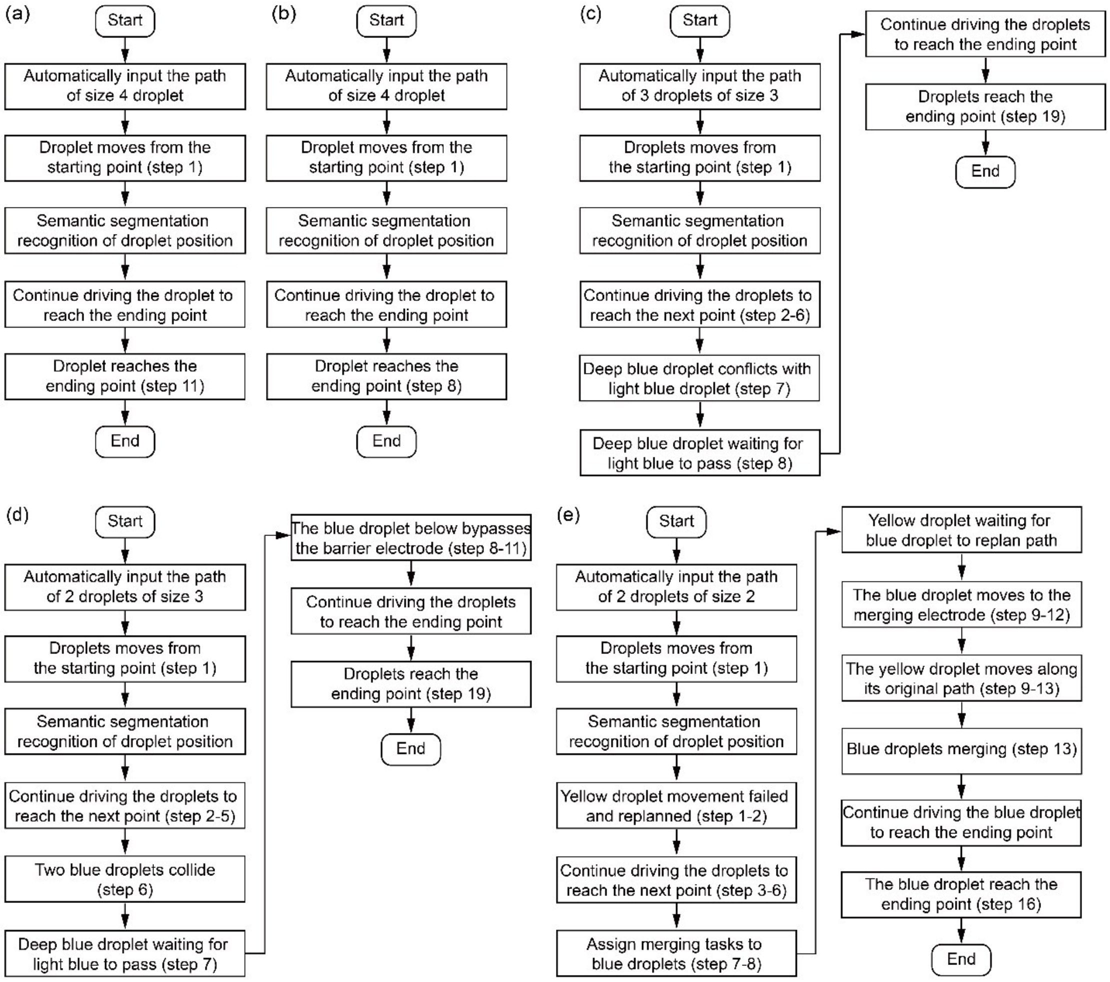

Fig. S4 Automated control workflow for droplet path planning in digital microfluidics. (a) 4U droplet path planning in four directions; (b) 4U droplet path planning in eight directions; (c) Multi-droplet path planning with conflict resolution; (d) Path planning in the presence of obstacle electrodes; (e) Path planning with dynamically inserted merging task.

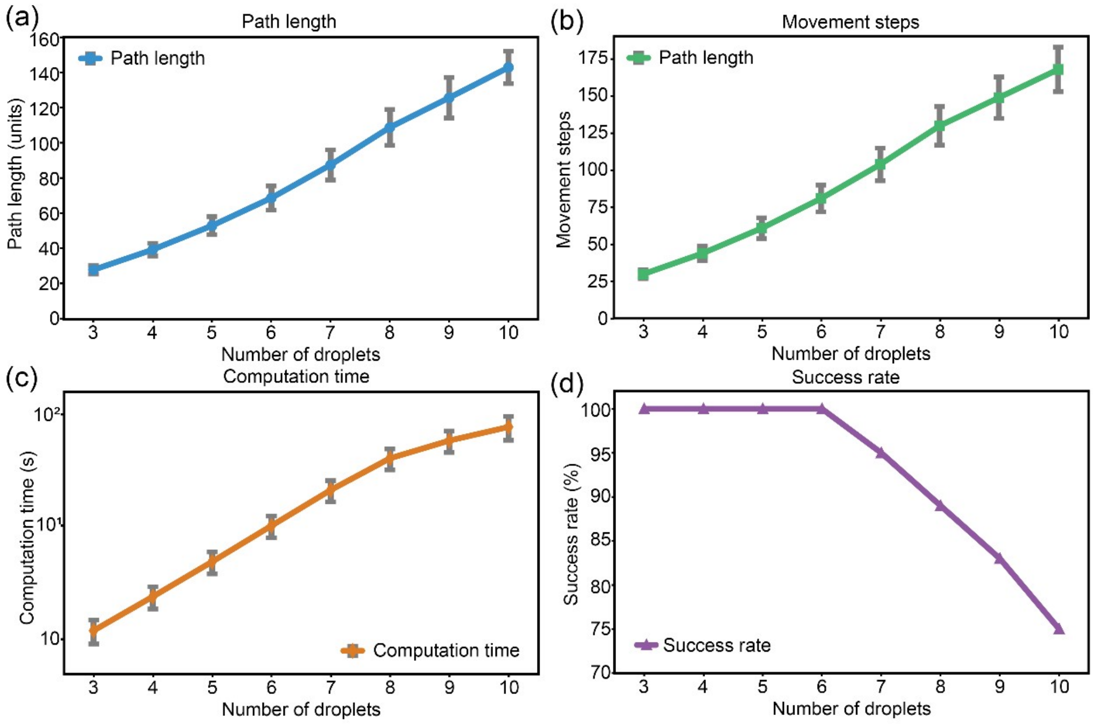

Fig. S5. Scalability analysis of the ATA algorithm for 3-10 droplets (1U, 5x18 chip, n=100). (a) Path length; (b) Movement steps; (c) Computation time; (d) Success rate.

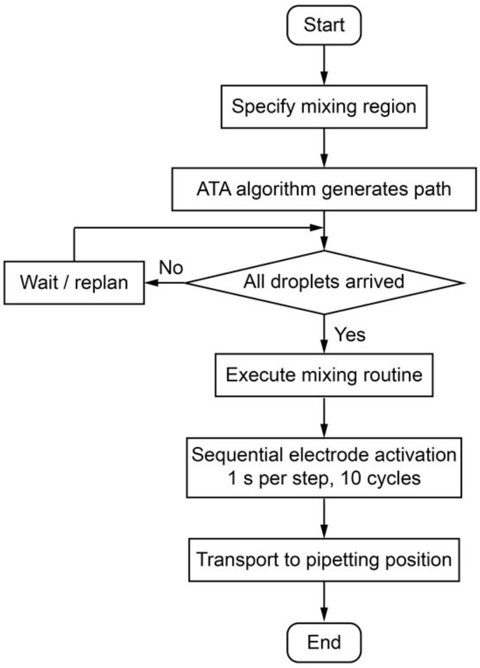

Fig. S6 Flowchart of the automated mixing operation workflow

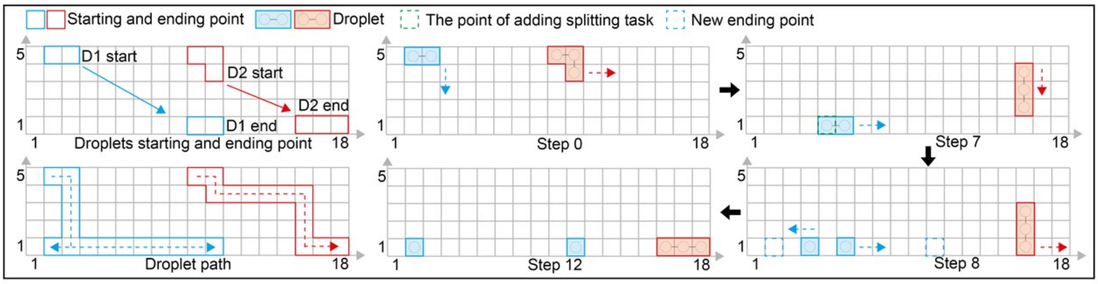

Fig. S7 Dynamic path planning following a splitting task insertion.

Table S4. Comparison of droplet routing algorithms for digital microfluidics

No.	Method	Year	Droplet Size	Multi-droplet	Algorithm Type	Dynamic Replanning	Feedback	Morphology Adaptation
1	Su et al.	2006	1U only	Yes	Heuristic search	No	No	Fixed
2	Cho & Pan	2008	1U only	Yes	ILP + Priority	No	No	Fixed
3	Huang & Ho	2009	1U only	Yes	Modified A*	No	No	Fixed
4	Roy et al.	2010	1U only	Yes	Network flow	No	No	Fixed
5	Pan et al.	2011	1U only	Yes	Ant Colony	Limited	No	Fixed
6	Huang et al.	2010	1U only	Yes	Contamination-aware	No	No	Fixed
7	Zhao & Chakrabarty	2012	1U only	Yes	Cross-contamination	No	No	Fixed
8	Lu et al.	2018	1U only	Yes	Flexible routing	Limited	No	Fixed
9	Liang et al.	2020	1U only	Yes	Deep RL	Yes	Vision-based	Fixed
10	Jiang et al.	2022	1U only	Yes	Evolutionary	Limited	No	Fixed
11	This work (TDMC)		Variable (1U-NU)	Yes	Adaptive-topology A*	Yes	Vision + Event	Yes

Note: 1U = one unit-cell droplet, typically occupying a single electrod. 4U = N unit-cell droplets, occupying 4 adjacent electrodes. All "Limited" methods require global recalculation, making them unsuitable for applications requiring rapid fault recovery or dynamic task insertion.

Reference

[1] Su, Fei, Sule Ozev, and Krishnendu Chakrabarty. Testing of Droplet-Based Microelectrofluidic Systems. ITC. Vol. 46. 2003.
[2] Cho, Minsik, and David Z. Pan. A high-performance droplet routing algorithm for digital microfluidic biochips. IEEE Transactions on Computer-Aided Design of Integrated Circuits and Systems 27.10 (2008): 1714-1724.
[3] Huang, Tsung-Wei, and Tsung-Yi Ho. A fast routability-and performance-driven droplet routing algorithm for digital microfluidic biochips. 2009 IEEE International Conference on Computer Design. IEEE, 2009.
[4] Roy, Pranab, Hafizur Rahaman, and Parthasarathi Dasgupta. A novel droplet routing algorithm for digital microfluidic biochips. Proceedings of the 20th symposium on Great lakes symposium on VLSI. 2010.
[5] Pan, Indrajit, et al. Ant colony optimization based droplet routing technique in digital microfluidic biochip. 2011 International Symposium on Electronic System Design. IEEE, 2011.
[6] Huang, Tsung-Wei, Shih-Yuan Yeh, and Tsung-Yi Ho. A network-flow based pin-count aware routing algorithm for broadcast-addressing EWOD chips. IEEE Transactions on Computer-Aided Design of Integrated Circuits and Systems 30.12 (2011): 1786-1799.
[7] Zhao, Yang, and Krishnendu Chakrabarty. Cross-contamination avoidance for droplet routing in digital microfluidic biochips. IEEE transactions on computer-aided design of integrated circuits and systems 31.6 (2012): 817-830.
[8] Lu, Guan-Ruei, et al. Flexible droplet routing in active matrix – based digital microfluidic biochips. ACM Transactions on Design Automation of Electronic Systems (TODAES) 23.3 (2018): 1-25.
[9] Liang, Tung-Che, and Zhanwei Zhong. Adaptive droplet routing in digital microfluidic biochips using deep reinforcement learning. Proceedings of the 37th International Conference on Machine Learning. 2020.
[10] Jiang, Chen, Rong-Quan Yang, and Bo Yuan. An evolutionary algorithm with indirect representation for droplet routing in digital microfluidic biochips. Engineering Applications of Artificial Intelligence 115 (2022): 105305.